Peertechz


CHEMISTRY GROUP

OPEN JOURNAL OF Chemistry OPEN ACCESS JOURNAL

ISSN: 2641-3051 DOI: https://dx.doi.org/10.17352/ojc

Research Article

# Optical spectroscopic analysis, supercapacitance, photocatalysis of $BaTi_xFe_{12-(4/3)x}O_{19}$ hexagonal nanoparticles

**Amina Ibrahim Ghoneim***

Physics Department, Faculty of Science, Tanta University, 31527 Tanta, Egypt

**Received:** 12 August, 2023
**Accepted:** 21 August, 2023
**Published:** 22 August, 2023

***Corresponding author:** Amina Ibrahim Ghoneim, Physics Department, Faculty of Science, Tanta University, 31527 Tanta, Egypt, Tel: +201032815387; Fax: +20403350804; E-mail: mona_ghoneim@yahoo.com, amina.ali@science.tanta.edu.eg

**ORCiD:** https://orcid.org/0000-0002-6489-2816

**Keywords:** $BaTi_xFe_{12-(4/3)x}O_{19}$ hexagonal nanoparticles; Raman; Photoluminescence; UV-VL spectra; Photocatalysis; Supercapacitance



https://www.peertechzpublications.org

Check for updates

## Abstract

Obviously, $BaTi_xFe_{12-(4/3)x}O_{19}$ Hexagonal nanocrystals are excellent candidates as photocatalysts in water purification, as well as using them as electrode materials for supercapacitors and energy storage applications. M-Type Hexagonal nanoparticles ($BaTi_xFe_{12-(4/3)x}O_{19}$, $0 \le x \le 1$) with the magneto-plumbite structure were formerly synthesized by co-precipitation procedure and investigated by several techniques such as XRD, FT-IR, Raman, Photoluminescence and UV-VL. XRD and FT-IR confirmed the structure, and Raman spectra showed 12 characterizing summits. Photoluminescence emission spectra indicated two summits at 448 and 501 nm. Optical UV-VL spectroscopic analysis parameters showed dependence on λ and *x*. Obviously, $BaTi_{0.75}Fe_{11}O_{19}$ nanocrystals as a sort of M-Type Hexagonal Ferrites showed excellent Photocatalytic activity on the Degradation of Organic Dyes like; Crystal Violet, Methyl Orange, … etc. Furthermore; these nanocrystals possess excellent electrochemical performance; which in turn introduces these materials for Supercapacitors Applications. Thus, the Photo-catalytic activity of $BaTi_{0.75}Fe_{11}O_{19}$ nanocrystals for the decolorization of Crystal Violet (**CV**) dye ($1 \times 10^{-5}$ M) illuminated excellent photocatalytic efficiency reaching ≈ 85%. On the other hand; $BaTi_{0.75}Fe_{11}O_{19}$ nanoparticles exhibited a specific capacitance of 1858 mF/g at 50 mV/s. The current study introduces promising applications of $BaTi_{0.75}Fe_{11}O_{19}$ nanoparticles as electrode materials for super capacitance and energy storage.

## Introduction

Hexagonal Nano-ferrites continue to be very substantial nanoparticles till the present time both from scientific, industrial as well as technological prospects ever since their discovery in 1950's [1]. Specification of such nanocrystals as Nano-hexaferrite stems from their ultrafine crystallite size or tiny nanoparticles size as well as their hexagonal crystalline structure. Lately, the most advanced research vistas have greatly focused on developing and synthesizing new unique nanoparticles with ultra-small grains for implementations in so many, diverse and expanding fields of technology such as shielding technology, magnetic recording media, spintronics, and microwave absorbing materials due to their excellent chemical stability, high thermal stability, non-toxicity, and extremely high corrosion resistivity [1-3]. Concomitantly, these M-Type hexagonal nanoparticles are utilized in industrial implementations in RADAR, wireless communication technologies, networks, Mobile technologies, and permanent magnets [4,5]. Furthermore, these M-type hexagonal nanoparticles have been also largely applied in versatile vistas like multiferroics [4,5]. Concomitantly, M-Type hexagonal nanoparticles are candidate targets as RADAR attenuating substances imputing their high permeability and high saturation magnetization [5-8]. Many research studies were concerned with the preparation of M-type hexagonal nanoparticles with diverse ions permutation utilizing diverse synthesis routes and varied characterizing techniques for the obtained Nano-samples [5-8]. Particle sizes, lattice parameters, saturation magnetization, coercivity, magneton number, and dislocation



**Citation:** Ghoneim AI (2023) Optical spectroscopic analysis, supercapacitance, photocatalysis of $BaTi_xFe_{12-(4/3)x}O_{19}$ hexagonal nanoparticles. Open Journal of Chemistry 9(1): 006-015. DOI: https://dx.doi.org/10.17352/ojc.000031

density of such hexagonal nano-ferrites were affected by synthesis conditions, thermal treatments, and substitution processes [5-8].

For **$BaTi_xFe_{12-(4/3)x}O_{19}$** Hexagonal nanocrystals; the introduction of $Ti^{4+}$ cations instead of $Fe^{3+}$ cations decreases the Band Gap Energy to the least value for $x$ = 0.75 (**$BaTi_{0.75}Fe_{11}O_{19}$** nanocrystals) which equals Eg = 3.3 eV. This in-tern increases its photocatalytic activity which is based on the hopping of electrons from the valency band to the conduction band, furthermore; for the small band gap of **$BaTi_{0.75}Fe_{11}O_{19}$** nanocrystals; electrons become more easily to move from the valency band to conduction band with high drift mobility so that free radicals are formed according to Figure 1 [9-15]:

Furthermore, the following equation demonstrates how the free radicals are formed:

$$e^- + O_2 \xrightarrow{h\nu} {}^{\bullet}O_2^-$$

$$e^- + H_2O \xrightarrow{h\nu} H^+ + {}^{\bullet}OH$$

In Nano-ferrites the electrons from the valency band are liberated to the conduction band leaving holes behind them in the valency band with the aid of photons from 100 W Tungsten lamb. Electrons in the conduction band unit with $O_2$ and OH give free radicals, which attack Crystal Violet (**CV**) dye with the help of photons from 100 W Tungsten lamp making degradation to **CV** dye easier giving degraded products in the form of $CO_2$ and $H_2O$ according to the following equation [16-18]:

$$O_2^{\bullet-} + CV^{\bullet+} \xrightarrow{h\nu} Degraded - \text{Products} - (H_2O + CO_2)$$

On the other hand; the substitution of $Ti^{4+}$ instead of $Fe^{3+}$ cations in **$BaTi_xFe_{12-(4/3)x}O_{19}$** Hexagonal nanocrystals decreases the Band Gap Energy to the least value for $x$ = 0.75 (**$BaTi_{0.75}Fe_{11}O_{19}$**) which equals Eg = 3.3 eV. The replacement of $Ti^{4+}$ cations with a smaller ionic radius (0.61 Å) instead of $Fe^{3+}$ cations with a larger ionic radius (0.64 Å) induces the decrease of hopping length between cations according to the following equation:

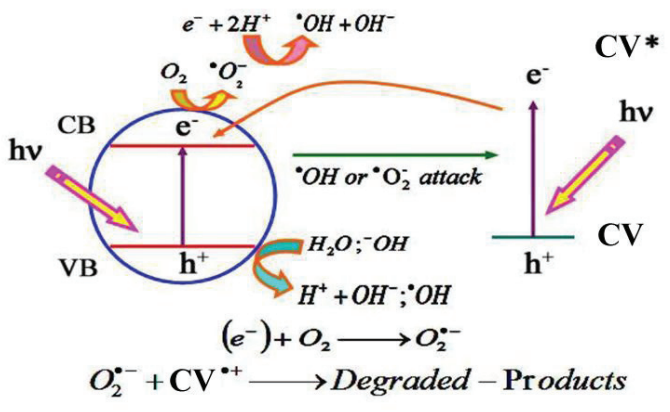


**Figure 1:** Photocatalysis mechanism of $BaTi_{0.75}Fe_{11}O_{19}$ for Degradation of Crystal Violet.

$$Fe^{3+} + Ti^{4+} \longrightarrow Fe^{4+} + Ti^{3+}$$

$$Fe^{4+} + Fe^{2+} \longrightarrow 2Fe^{3+}$$

Thus the oxidation and reduction processes are really occurring all the interaction time in **$BaTi_xFe_{12-(4/3)x}O_{19}$** Hexagonal nanocrystals and the least band gap energy accompanied with the least hopping length is a fact chemical property for $x$ = 0.75 (**$BaTi_{0.75}Fe_{11}O_{19}$** nanocrystals). These natural, active, and fast oxidation and reduction processes occurring in **$BaTi_{0.75}Fe_{11}O_{19}$** nanocrystals are the basis for the supercapacitor's electrochemical performance indicating that **$BaTi_{0.75}Fe_{11}O_{19}$** nanocrystals are excellent candidates for supercapacitor and energy storage applications [19-28]. Whereas; Barium element possesses only one oxidation state ($Ba^{2+}$ cations) and it is a paramagnetic cation.

The current investigation is devoted to synthesizing M-type hexagonal **$BaTi_xFe_{12-(4/3)x}O_{19}$** nanoparticles by the chemical co-precipitation method. The samples were characterized using X-ray diffraction (XRD), FTIR, Raman, Photoluminescence, and UV-VL spectral analysis. Furthermore, their Photocatalysis in the degradation of Crystal Violet (**CV**) and electrochemical performance, Supercapacitance were also investigated.

## Experimental section

### Chemical materials

All chemical reagents were extra-high purity AnalaR (AR) grade and used as received without further purification, and were purchased from Sigma-Aldrich. Stoichiometric proportion amounts of the high purity $Ba(NO_3)_2$, $Ti(C_{12}H_{28}O_4)$, $Fe(NO_3)_3$ -$9H_2O$ and NaOH were used. All aqueous solutions were freshly prepared using high-purity distilled water.

### Materials synthesis

M-type hexagonal **$BaTi_xFe_{12-(4/3)x}O_{19}$** nanoparticles, $x$ = 0, 0.125, 0.25, 0.375, 0.5, 0.75, and 1 were prepared by the chemical co-precipitation method according to the equation [3];

$Ba(NO_3)_2$ + $x$ $Ti(C_{12}H_{28}O_4)$ + (12−(4)/(3)$x$) $Fe(NO_3)_3$-$9H_2O$ + (38-4$x$) NaOH → **$BaTi_xFe_{12-(4/3)x}O_{19}$** + (38-4$x$)$NaNO_3$ + 4$x$$(CH_3)_2CHOH$ + (127-16$x$)$H_2O$

Stoichiometric proportion amounts of the high purity AnalaR (AR) grade $Ba(NO_3)_2$, $Ti(C_{12}H_{28}O_4)$, and $Fe(NO_3)_3$-$9H_2O$ were dissolved in distilled water and kept at about 10 °C for one hour (h). The reactants were mixed and constantly stirred using a magnetic stirrer for 10 min. The NaOH solution was added drop-wise where the pH of the mixed solution was constantly monitored as pH ≈ 13. Then the solution was heated and maintained at 90 °C for 2 h under continuous stirring till the precipitation occurred. The precipitates were thoroughly washed with distilled water until the washings become free from sodium Nitrate. The precipitates were dried for a few days at room temperature. Then the samples were thoroughly ground in an agate mortar to obtain a fine powder. Thereafter, the samples were annealed for 20 h at 1200 °C and then slowly cooled to room temperature. The samples were ground to a fine



**Citation:** Ghoneim AI (2023) Optical spectroscopic analysis, supercapacitance, photocatalysis of $BaTi_xFe_{12-(4/3)x}O_{19}$ hexagonal nanoparticles. Open Journal of Chemistry 9(1): 006-015. DOI: https://dx.doi.org/10.17352/ojc.000031

powder and annealed again at 1200 °C for 20 h and then slowly cooled to room temperature. Finally, the nanoparticle samples were ground in an agate mortar to fine powder [3].

## Characterization

**Materials characterization:** M-type hexagonal $BaTi_xFe_{12-(4/3)x}O_{19}$ nanoparticles, (x = 0, 0.125, 0.25, 0.375, 0.5, 0.75, and 1) were prepared by the chemical co-precipitation strategy; as reported earlier by Amer, et al. (2015) [3]. These samples have been characterized by an X-ray diffractometer (GNR APD 2000 Pro step scan type and CuKα1 radiation with wavelength λ = 1.540598 Å). FT-IR spectra for all nano-samples were exhibited by using Bruker-Tensor-27- FT-IR - type Spectrometer in the range 200 to 2000 $cm^{-1}$, at room temperature. Raman spectra were measured by JASCO NRS-3100 micro-spectrometer with an excitation radiation of 532 nm laser. Room temperature photoluminescence spectroscopy (KIMMON KOHA, Tokyo, Japan, excitation wavelength, λ = 325 nm). UV–vis spectra were registered using JASCO V570 UV–VIS-NIR scan-type spectrophotometer in the wavelengths 190–1200 nm at room temperature.

**Photocatalytic activity:** Photocatalytic features for $BaTi_{0.75}Fe_{11}O_{19}$ nanocrystals were scrutinized via photo-disintegration of the simulated dye wastewater of Crystal Violet (**CV**) dye solution under VL irradiation utilizing 100 Watt Tungsten lamp fixed at ~ 10 cm distance, as illustrated earlier by Ghoneim (2021) [29]. Aqueous suspension of **CV**-dye ($1 \times 10^{-5}$ M) and $BaTi_{0.75}Fe_{11}O_{19}$ nanocrystals as photo-catalysts (0.1 g) were placed in a glass beaker. Prior to irradiation, each suspension was stirred in the dark for 2 hrs to establish adsorption-desorption equilibrium (between photo-catalysts and dye), followed by VL irradiation utilizing 100 Watt Tungsten lamp fixed at ~ 10 cm distance. At time spans (20 min), 3 mL of suspension was taken from the beaker, and then filtered to remove solid powders. Thence, solutions were analyzed by UV–VIS scan-type photometer in the wavelengths 190 – 1200 nm at ambient temperature to obtain relative concentration variations of solution. UV–vis spectra were registered using SPECTRO UV–VIS DUAL BEAM 8 AUTO CELL UVS-2700 scan-type spectrophotometer in the wavelengths 190–1200 nm at ambient temperature. Curve about concentration variations ($C/C_o$) as a function of time was plotted, where **C** presented the concentration of **CV** at each time interval and $C_o$ was the initial concentration of **CV** after reaching adsorption-desorption equilibrium [29-31].

**Electrochemical characterization:** Electrochemical Performance measurements were carried out by a three-electrode cell system using a Solartron SI 1286 electrochemical workstation in 1 M KOH electrolyte solution at room temperature. The working electrode was prepared by mixing $BaTi_{0.75}Fe_{11}O_{19}$ nano-hexa-ferrites into a solution of isopropyl alcohol, water, and nafion (volume ratio 5:5:0.1) with the help of ultra-sonication (10 min) to form the homogeneous solution. From the mixed solution, a 10 µL amount of liquid was dropped on a glassy carbon electrode (GCE) (3 mm diameter) and the liquid was evaporated in air to dry the active materials. In three-electrode measurements, $BaTi_{0.75}Fe_{11}O_{19}$ Hexagonal nanoparticles, platinum (Pt) wire, and Hg/HgO work as working electrode, counter electrode, and reference electrode, respectively. Cyclic voltammetry (**CV**) and galvanostatic charging/discharging measurements were carried out to investigate the electrochemical performance of $BaTi_{0.75}Fe_{11}O_{19}$ Hexagonal nanoparticles electrode for super-capacitance SCs applications.

# Results and discussion

## X-Ray Diffraction (XRD) spectra analysis

X-ray diffraction patterns (XRD) and their initial analysis for M-type hexagonal $BaTi_xFe_{12-(4/3)x}O_{19}$ nanoparticles, (x = 0, 0.125, 0.25, 0.375, 0.5, 0.75 and 1) were investigated and published earlier by Amer, et al. (2015) [3] as indicated in Figure 2. XRD plots in Figure 2 proved that the samples have single-phase M-type hexagonal structure [3], which was affirmed by matching with JCPDS data (Card nos. 00-027-1029, 00-007-0276 and 01-079-1411).

Table 1 illustrates the relation between the unit cell volume $V_{cell}$ and $Ti^{4+}$ content *x*.

Unit cell volume for $BaTi_xFe_{12-(4/3)x}O_{19}$ M-type hexagonal nanoparticles has been calculated from the relation [31,32];

$$V_{cell} = \frac{\sqrt{3}}{2} a^2 c$$

It is clear that $V_{cell}$ for these nanoparticles increases with *x*; (Table 1).

Dislocation density δ was calculated by using the relation [33]:

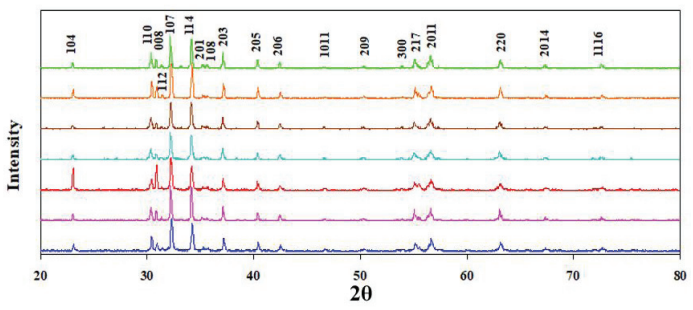


**Figure 2:** XRD plots of $BaTi_xFe_{12-(4/3)x}O_{19}$ nanoparticles, (x = 0, 0.125, 0.25, 0.375, 0.5, 0.75 and 1).

**Table 1:** Unit cell volume $V_{cell}$, interchain distance **r**, distortion parameter **g** and dislocation density **δ**; error = ± 0.002.

| *x* | V (Å³) | r (Å) | g | δ ($nm^{-2}$) |
|---|---|---|---|---|
| 0 | 693.15 | 3.4595 | 0.00843 | 0.0002862 |
| 0.125 | 693.25 | 3.4681 | 0.00845 | 0.0002863 |
| 0.25 | 694.38 | 3.4638 | 0.00905 | 0.0003286 |
| 0.375 | 694.41 | 3.4679 | 0.00965 | 0.0003741 |
| 0.5 | 694.51 | 3.4638 | 0.01025 | 0.0004221 |
| 0.75 | 694.15 | 3.4575 | 0.01203 | 0.0005841 |
| 1 | 697.03 | 3.4678 | 0.01087 | 0.0004733 |



**Citation:** Ghoneim AI (2023) Optical spectroscopic analysis, supercapacitance, photocatalysis of $BaTi_xFe_{12-(4/3)x}O_{19}$ hexagonal nanoparticles. Open Journal of Chemistry 9(1): 006-015. DOI: https://dx.doi.org/10.17352/ojc.000031

$$\delta = \frac{1}{R^2};$$

Where R is the crystallite size.

The inter-chain separation **r** and the distortion parameter **g** have been calculated using the relations [33]:

$$r = \frac{5\lambda}{8\sin\theta}$$

$$g = \frac{\frac{\beta_1}{2}}{\tan\theta}$$

Table 1 displays the reliance of **r, g**, and δ with the change of $Ti^{4+}$ content **x**.

It is clear that r, g, and δ increase with $Ti^{4+}$ content *x* imputing to the substitution process.

## Elastic Parameters

FT-IR spectra from 200 to 2000 $cm^{-1}$ and their initial analysis for M-type hexagonal **$BaTi_xFe_{12-(4/3)x}O_{19}$** nanoparticles, (x = 0, 0.125, 0.25, 0.375, 0.5, 0.75 and 1) were investigated and published earlier by Amer et al (2015) [3].

Elastic Parameters extracted from FT-IR Spectra are presented in the following:

For investigating the elastic attributes of these nanocrystals, elastic moduli as Young's modulus E, bulk modulus K, and modulus of rigidity G are concluded using the formulas [34-36]:

$$\text{Young's Modulus } E = \frac{(C_{11}-C_{12})(C_{11}+2C_{12})}{(C_{11}+C_{12})}$$

$$\text{Rigidity Modulus } G = \frac{E}{2(\sigma+1)}$$

$$\text{Bulk Modulus } K = \frac{1}{3}(C_{11}+2C_{12})$$

Where $C_{11}$ and $C_{12}$ are stiffness constants, and σ is Poisson's ratio [34-36].

Table 2 illuminates that the three moduli: E, K, and G change nonlinearly with *x*.

## Wave velocities

Longitudinal elastic wave velocity ($V_L$), shear wave velocity ($V_S$), and the mean wave velocity ($V_m$) are concluded from the formulations [34,35]:

$$\text{Longitudinal Velocity } V_L = \left(\frac{C_{11}}{D_x}\right)^{\frac{1}{2}},$$

$$\text{Shear Velocity } V_S = \left(\frac{G_o}{D_x}\right)^{\frac{1}{2}},$$

The mean wave velocity $V_m$ can be deduced using the relation: $\frac{3}{V_m^3} = \frac{1}{V_L^3} + \frac{2}{V_S^3}$,

Where $G_o$ is the rigidity modulus with zero pore fraction. Table 3 illustrates the variation of $V_L$, $V_S$, and $V_m$ against *x*. It is plain that $V_L$, $V_S$, and $V_m$ increase with $Ti^{4+}$ ion increase *x*. Obviously, the dependence of density $D_x$ on both elastic moduli and wave velocities influences their values. The elastic moduli and wave velocities rise to reflect the variation of crystal structure and prove that the wave velocities are strongly correlated with the nanocrystal's density [34,35,37].

## Raman spectra

Raman spectra investigated for M-type hexagonal **$BaTi_xFe_{12-(4/3)x}O_{19}$** nanoparticles, (x = 0, 0.125, 0.25, 0.375, 0.5, 0.75 and 1) at room temperature are shown in Figure 3. In the frequency range of 100-800 $cm^{-1}$ for **$BaTi_xFe_{12-(4/3)x}O_{19}$** nanoparticles, there appears 12 summits at frequencies ν ~ 173, 183, 215, 282, 318, 345, 415, 470, 521, 616, 686 and 715 $cm^{-1}$. These results agree well with the previously earlier published work [1,2]. Summits ν in between 318 – 715 $cm^{-1}$ are essentially related to the oscillations of iron polyhedra. Summits at 345, 470, and 616 $cm^{-1}$ are due to vibrations of Fe1(2a)-O6 octahedra. Summits at 318, 521 and 616 $cm^{-1}$ are due to vibrations of $Fe4(4f_{VI})/Ti4(4f_{VI})$-O6 octahedra. Summits at 415, 521 and 616 $cm^{-1}$ are due to vibrations of Fe5(12k)/Ti5(12k)-O6 octahedra. Summits at 686 $cm^{-1}$ modes are related to oscillations of the

**Table 2:** Elastic moduli; Young's modulus E, modulus of rigidity G and bulk modulus K; error = ± 0.002.

| *x* | E (GPA) | G (GPA) | K (GPA) |
|---|---|---|---|
| 0 | 206.91 | 111.07 | 60.65 |
| 0.125 | 207.48 | 110.48 | 61.65 |
| 0.25 | 208.81 | 110.89 | 62.31 |
| 0.375 | 206.52 | 109.31 | 61.98 |
| 0.5 | 209.75 | 110.58 | 63.36 |
| 0.75 | 208.41 | 109.38 | 63.47 |
| 1 | 209.32 | 109.55 | 64.05 |

**Table 3:** Longitudinal elastic wave velocity ($V_L$), shear wave velocity ($V_S$) and mean wave velocity; error = 0.002.

| *x* | $V_L \times 10^3$ (m/s) | $V_S \times 10^3$ (m/s) | $V_m \times 10^3$ (m/s) |
|---|---|---|---|
| 0 | 6.728 | 4.736 | 5.139 |
| 0.125 | 6.722 | 4.737 | 5.138 |
| 0.25 | 6.777 | 4.777 | 5.182 |
| 0.375 | 6.748 | 4.758 | 5.161 |
| 0.5 | 6.801 | 4.797 | 5.203 |
| 0.75 | 6.803 | 4.801 | 5.206 |
| 1 | 6.852 | 4.835 | 5.245 |



**Citation:** Ghoneim AI (2023) Optical spectroscopic analysis, supercapacitance, photocatalysis of $BaTi_xFe_{12-(4/3)x}O_{19}$ hexagonal nanoparticles. Open Journal of Chemistry 9(1): 006-015. DOI: https://dx.doi.org/10.17352/ojc.000031

bipyramidal anion Fe2(2b)-O5 sublattices, and Summits at 715 $cm^{-1}$ are related to oscillations of the tetrahedral anion Fe3($4f_{IV}$)/Ti3($4f_{IV}$)-O4 sublattices. The contribution of the $Ti^{4+}$ diamagnetic cations in the nanocrystals leads to a shift and distortion of the Raman spectra [1,2].

## Photoluminescence spectra

Photoluminescence (PL) spectroscopy was measured at room temperature to investigate the optical property of M-type hexagonal $BaTi_xFe_{12-(4/3)x}O_{19}$ nanoparticles, (x = 0, 0.125, 0.25, 0.375, 0.5, 0.75 and 1) as shown in Figure 4. Furthermore, it was further studied to survey the efficiency of photocatalytic charge carrier's generation and mobility [38]. It gives information about the ability to separate photo-generate electrons-holes in $BaTi_xFe_{12-(4/3)x}O_{19}$ nanoparticles. Figure 4 displays the PL emission spectra of $BaTi_xFe_{12-(4/3)x}O_{19}$ nanoparticles with summits at 448 and 501 nm wavelengths as the excitation sources. The photoluminescence peaks are mainly the result of electron-hole pairs recombination. Obviously, the emission summits position is nearly unchanged. It could be concluded that M-type hexagonal $BaTi_xFe_{12-(4/3)x}O_{19}$ nanoparticles should possess the highest photocatalytic activity, which is in good agreement with the experiment of Photocatalytic Activity illustrated later.

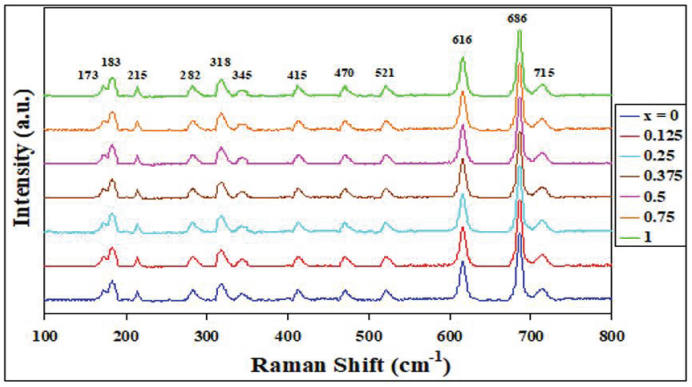


**Figure 3:** Raman spectra at room temperature for M-type hexagonal $BaTi_xFe_{12-(4/3)x}O_{19}$ nanoparticles, (x = 0, 0.125, 0.25, 0.375, 0.5, 0.75, and 1).

## Optical UV-VL spectroscopic analysis

UV-VL absorbance (A) as well as, the reflectance R and the transmittance T spectral plots for M-type hexagonal $BaTi_xFe_{12-(4/3)x}O_{19}$ nanoparticles, (x = 0, 0.125, 0.25, 0.375, 0.5, 0.75 and 1), were illuminated in Figure 5. Where the transmittance T has been concluded by using the formula [39]:

$$A + R + T = 1$$

The absorption coefficient α (ν) as presented in Figure 6 for $BaTi_xFe_{12-(4/3)x}O_{19}$ nanoparticles with increasing *x* can be confirmed using the formula [39]:

$$\alpha(\nu) = 2.303\left(\frac{A}{d}\right),$$

Where A is the absorbance, and d is the nano-sample thickness.

Absorption edge and band-gap energy (Eg) were derived from [40-45]:

$$(\alpha \cdot h\nu) = B\left(h\nu - E_g\right)^n,$$

Where hν is the photon's energy, α is the optical coefficient of absorbed power and B is a transmission constant of electrons [41,42]. The absorption peak observed at 580 nm corresponds to M-type hexagonal $BaTi_xFe_{12-(4/3)x}O_{19}$ nanoparticles, as illustrated in Figures 5,7 clarifies the relation between $(\alpha h\nu)^2$

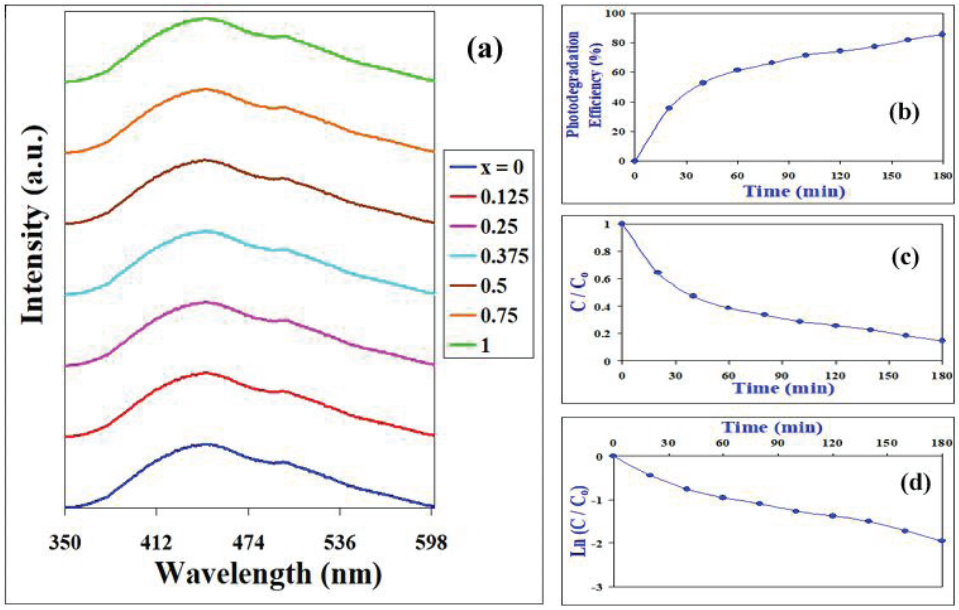


**Figure 4:** (a) Photoluminescence (PL) spectra of M-type hexagonal $BaTi_xFe_{12-(4/3)x}O_{19}$ nanoparticles, (x = 0, 0.125, 0.25, 0.375, 0.5, 0.75 and 1), (b-d) Photo-catalytic efficiency and Photo-Degradation of **CV** ($1 \times 10^{-5}$ M) utilizing $BaTi_{0.75}Fe_{11}O_{19}$ nanocrystals as photo-catalysts, with time duration 20 min.



**Citation:** Ghoneim AI (2023) Optical spectroscopic analysis, supercapacitance, photocatalysis of $BaTi_xFe_{12-(4/3)x}O_{19}$ hexagonal nanoparticles. Open Journal of Chemistry 9(1): 006-015. DOI: https://dx.doi.org/10.17352/ojc.000031

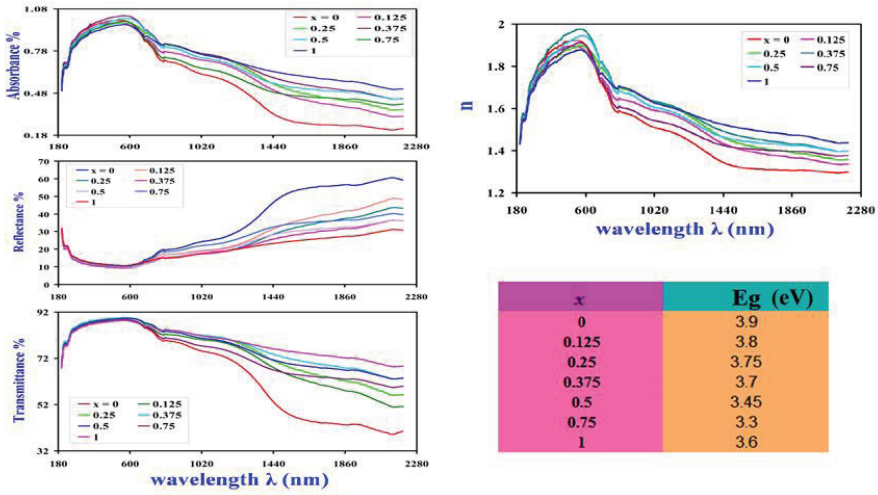


| x | Eg (eV) |
|---|---|
| 0 | 3.9 |
| 0.125 | 3.8 |
| 0.25 | 3.75 |
| 0.375 | 3.7 |
| 0.5 | 3.45 |
| 0.75 | 3.3 |
| 1 | 3.6 |

**Figure 5:** Absorbance A, Reflectance R, Transmittance T, refractive index (n), and optical band gap energy (Eg) for $BaTi_xFe_{12-(4/3)x}O_{19}$ nanoparticles.

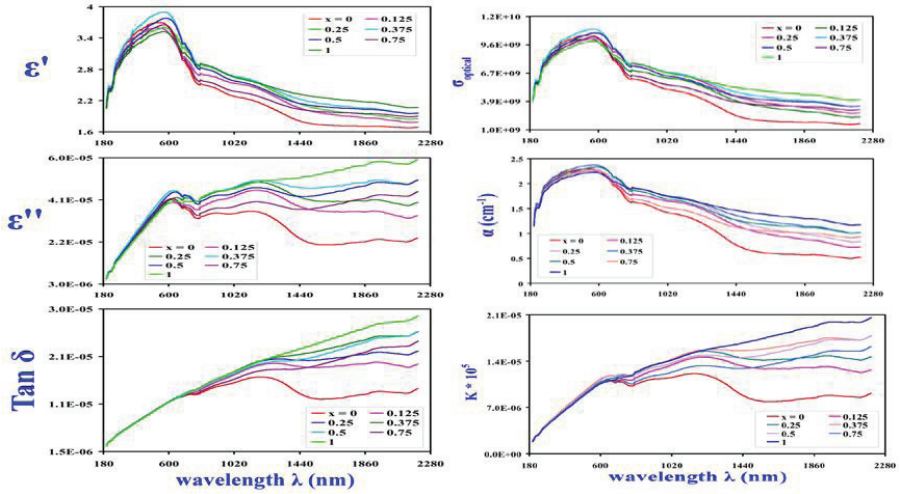


**Figure 6:** Variation of ε' the real part and ε" the imaginary part of the dielectric constant, dielectric loss Tan δ, optical conductivity ($\sigma_{optical}$), absorption coefficient α (ν) and extinction coefficient K($cm^{-1}$) with λ.

and photon energy (hν (eV)). It is explicit that the UV cut-off trend is reversible to the optical energy gap of nanocrystals with varying *x* at which it is acquired from plot-tangent (Figure 7). The absorption detected edge in the visible section for these nanomaterials is in synchrony with the electron hopping from O-2p level into Fe-3d level for these nanocrystals [41,42].

The decrease of Eg with *x* (Fig. 5) reflects the substitution process as well as the increase of lattice spacing and oxygen ion concentration in the sample [40,43,45].

The extinction coefficient as shown in Figure 6 is usually calculated using the well-known relation [39]: $K = \frac{\alpha\lambda}{4\pi}$

Substantially, Refractive index n was derived from reflectance R [39,40]; according to:

$$R = \frac{(n-1)^2}{(n+1)^2}$$

Changing of n with UV-photon wavelength λ (nm) was demonstrated in Figure 5. Optical conductivity ($\sigma_{optical}$) demeanor with λ for the nanocrystals was displayed in Figure 6, whereas the distinctive evaluation of $\sigma_{optical}$ was concluded from the formula [39,40]:

$$\sigma_{Optical} = \frac{\alpha \cdot n \cdot C}{4\pi},$$

Where α is the optical coefficient of absorbed power and C is light velocity. The optical conductivity ($\sigma_{optical}$) for all the annealed nanoparticles showed a sharp increase with λ up to ~ 580 nm and decreases thereafter in a gradual manner. Complex dielectric constant has real and imaginary parts that are explained [39,44] using the expressions:

$$\varepsilon' = n^2 - K^2 \text{ and } \varepsilon'' = 2nK$$

Regarding the reliance of ε′ with λ (nm) as indicated in Figure 6; an explicit dispersion of ε′ was observed for all nano-samples, i.e., ε′ values are high at long wavelengths and



**Citation:** Ghoneim AI (2023) Optical spectroscopic analysis, supercapacitance, photocatalysis of $BaTi_xFe_{12-(4/3)x}O_{19}$ hexagonal nanoparticles. Open Journal of Chemistry 9(1): 006-015. DOI: https://dx.doi.org/10.17352/ojc.000031

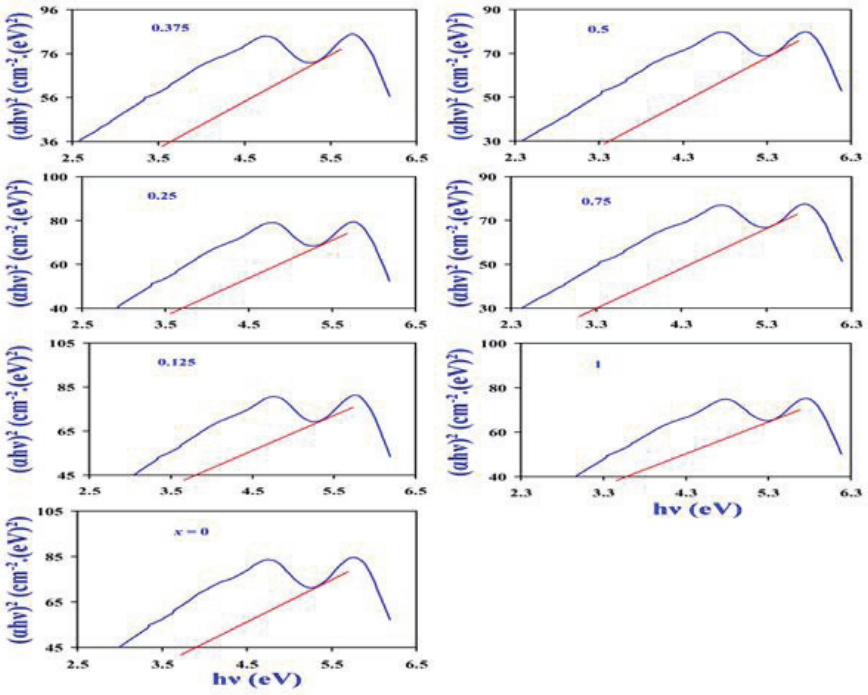


**Figure 7:** The optical energy gap for $BaTi_xFe_{12-(4/3)x}O_{19}$ nanoparticles.

shows a peaking behavior at ~ 580 nm and gradually decrease thereafter. Whilst ε" gradually increases with λ as shown in Figure 6. Dielectric loss tangent (Tan δ) was calculated from the following expression [46]:

$$Tan\delta = \frac{\varepsilon''}{\varepsilon'}$$

It is clear that Tan δ increase with λ (nm) as indicated in Figure 4.

## Photocatalytic Activity of $BaTi_{0.75}Fe_{11}O_{19}$ nanocrystals

The photo-catalytic activity of **$BaTi_{0.75}Fe_{11}O_{19}$** nanocrystals for the sequent decolorization of Crystal Violet (**CV**) dye ($1 \times 10^{-5}$ M) in aqueous solution under VL irradiation via 100-Watt Tungsten lamp fixed at ~ 10 cm distance, investigated with an increase of time intervals up to 180 minutes, (time duration is 20 min) were affirmed in Figure 4. All of the catalytic disintegration reactions followed pseudo-first-order kinetics, confirmed with the plot of ($C/C_o$) against time (min), and the plot of ln ($C/C_o$) against contact time (min), (Figure 4). Clearly, **CV** concentrations decrease with the increase of stirring time affirming the photocatalytic activity of **$BaTi_{0.75}Fe_{11}O_{19}$** nanocrystals. Photo-Degradation Efficiency was obtained by the following equation [29-31]:

$$Degradation - Efficiency = \left(1 - \frac{C}{C_o}\right) \times 100$$

Photo-catalytic efficiency of **$BaTi_{0.75}Fe_{11}O_{19}$** nanocrystals for **CV** decolorization was easily shown in Figure 4, confirming the increase of their activity in the photo-degradation of **CV** dye, and referring to how excellent quality will be the outcome of $H_2O$ produced by this strategy. Obviously; the Photo-catalytic activity of **$BaTi_{0.75}Fe_{11}O_{19}$** nanocrystals for the decolorization of Crystal Violet (**CV**) dye ($1 \times 10^{-5}$ M) illuminated excellent photocatalytic efficiency reaching ≈ 85%.

## Electrochemical characterization of $BaTi_{0.75}Fe_{11}O_{19}$

The electrochemical performance of **$BaTi_{0.75}Fe_{11}O_{19}$** nanoparticles was investigated by Cyclic Voltammetry (**CV**) and tested in 1 M KOH electrolytes at room temperature. **CV** curve of **$BaTi_{0.75}Fe_{11}O_{19}$** nanoparticles electrode was determined at scan rates of (50 mV/s) in the potential range of -0.5–0.5 V as shown in Figure 8. **$BaTi_{0.75}Fe_{11}O_{19}$** nanoparticles electrode exhibited larger **CV** curve area, indicating its superior electrochemical performance, where **CV** curve showed redox peaks. The nearly rectangular shape of the cyclic voltammetry curve revealed that electric double-layer capacitance was dominant [47-50]. This represents that the redox reactions on the electrode surface were fast and reversible. The specific capacitance of **$BaTi_{0.75}Fe_{11}O_{19}$** nanoparticle electrode materials equals 1858 mF/g, proving that **$BaTi_{0.75}Fe_{11}O_{19}$** nanoparticles are electrode materials for Supercapacitance applications. The electrical behavior of electrode materials for SCs applications was investigated by electrochemical impedance spectroscopy (EIS). Figure 8 shows the Nyquist plots for **$BaTi_{0.75}Fe_{11}O_{19}$** nanoparticles in the frequency range from 1.0 Hz to 20 kHz. Solution resistance (Rs) equals 22 Ω. There is a direct proportionality between Z'' and Z' giving diffusive resistance [47-50].

## Conclusion

M-Type **$BaTi_xFe_{12-(4/3)x}O_{19}$** nanoparticles were synthesized by co-precipitation strategy and examined using XRD, FT-IR, Raman, Photoluminescence, and UV-VL. XRD and FT-IR



**Citation:** Ghoneim AI (2023) Optical spectroscopic analysis, supercapacitance, photocatalysis of $BaTi_xFe_{12-(4/3)x}O_{19}$ hexagonal nanoparticles. Open Journal of Chemistry 9(1): 006-015. DOI: https://dx.doi.org/10.17352/ojc.000031

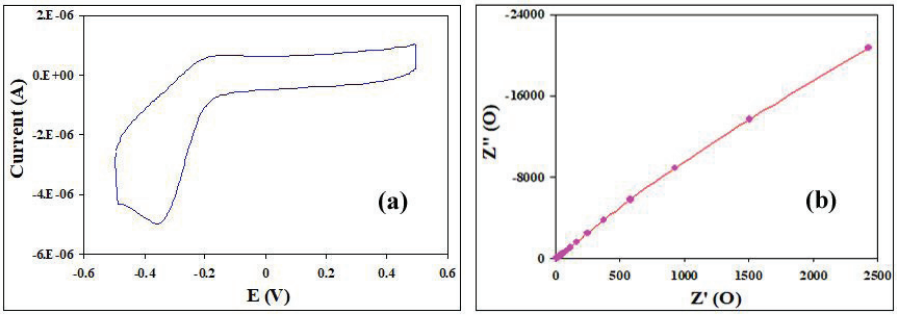


**Figure 8:** The electrochemical performance of $BaTi_{0.75}Fe_{11}O_{19}$ nanoparticles electrode. (a) CV curves at a scan rate of 50 mV/s and (b) Nyquist plot of $BaTi_{0.75}Fe_{11}O_{19}$ nanoparticles.

confirmed their M-Type Hexagonal structure, and Raman spectra showed 12 characterizing summits. Photoluminescence emission spectra of $BaTi_xFe_{12-(4/3)x}O_{19}$ nanoparticles indicated two summits at 448 and 501 nm wavelengths as the excitation sources. Band gap energy Eg decreases with $Ti^{4+}$ ion content *x* reflecting the substitution process as well as the increase of lattice spacing and oxygen ion concentrations in the samples. All the optical UV-VL spectroscopic analysis parameters showed reliance on λ and *x*. The photocatalytic activity of $BaTi_{0.75}Fe_{11}O_{19}$ nanocrystals was acquired throughout the decolorization of Crystal Violet (**CV**) dye ($1 \times 10^{-5}$ M) in aqueous solution under VL irradiation via 100 Watt Tungsten lamp fixed at ~ 10 cm distance. Cyclic voltammetry for studying super capacitance of $BaTi_{0.75}Fe_{11}O_{19}$ nanoparticles in 1.0 M KOH electrolyte solution. $BaTi_{0.75}Fe_{11}O_{19}$ nanoparticles exhibited a specific capacitance of 1858 mF/g at 50 mV/s. The nearly rectangular shape of the cyclic voltammetry curve revealed that electric double-layer capacitance was dominated. The current study introduces a promising application of $BaTi_{0.75}Fe_{11}O_{19}$ nanoparticles as electrode materials for super capacitance and energy storage. Nyquist plots for $BaTi_{0.75}Fe_{11}O_{19}$ nanoparticles were taken in the frequency range from 1.0 Hz to 20 kHz, and solution resistance (Rs) equals 22 Ω.

## References


1. Verma S, Chawla A, Pushkarna I, Singh A, Godara SK. Understanding the phase evolution with temperature in pure ($BaFe_{12}O_{19}$) and zinc-zirconium co-doped barium hexaferrite ($BaZnZrFe_{10}O_{19}$) samples using Pawley and Rietveld analysis. Materials Today Communications. 2021; 27: 102291. https://doi.org/10.1016/j.mtcomm.2021.102291

2. Jiang X, Jia H, Wu C, Yu Z, Luo H. Cation distribution and magnetic characteristics of textured $BaFe_{12-x}Sc_xO_{19}$ hexaferrites: Experimental and theoretical evaluations. Journal of Alloys and Compounds. 2020; 835: 155202. https://doi.org/10.1016/j.jallcom.2020.155202

3. Amer M, Meaz T, Attalah S, Ghoneim A Structural and magnetic studies of $Ti^{4+}$ substituted M-type $BaFe_{12}O_{19}$ hexa-nanoferrites. Materials Science in Semiconductor Processing. 2015; 40: 374–382. http://dx.doi.org/10.1016/j.mssp.2015.07.007

4. Vinnik D, Zhivulin V, Starikov A, Gudkova S, Trofimov E. Influence of titanium substitution on structure, magnetic and electric properties of barium hexaferrites BaFe12-xTixO19. Journal of Magnetism and Magnetic Materials. 2019. https://doi.org/10.1016/j.jmmm.2019.166117

5. Goldman A. Marcel Dekker Inc., New York. Modern Ferrite Technology (Online) 1993.

6. Godara S, Kaur V, Chuchra K, Narang S, Singh G. Impact of $Zn^{2+}$-$Zr^{4+}$ substitution on M-type Barium Strontium Hexaferrite's structural, surface morphology, dielectric and magnetic properties. Results in Physics. 2021; 22: 103892. https://doi.org/10.1016/j.rinp.2021.103892

7. Thang P, Tiep N, Ho T, Co N, Hong N. Electronic structure and multiferroic properties of (Y, Mn)-doped barium hexaferrite compounds. Journal of Alloys and Compounds. 2021; 867: 158794. https://doi.org/10.1016/j.jallcom.2021.158794

8. Kumar S, Guha S, Supriya S, Pradhan L, Kar M . Correlation between Crystal Structure Parameters with Magnetic and Dielectric Parameters of Cu-Doped Barium Hexaferrite. Journal of Magnetism and Magnetic Materials. 2019. https://doi.org/10.1016/j.jmmm.2019.166213

9. Kalikeri S, Kodialbail V. Visible light active Bismuth ferrite embedded TiO2 nanocomposite structures for dye mineralization by photocatalysis -A strategy to harness solar energy for remediation of water contaminated with mixture of dyes. Surfaces and Interfaces. 2023; 36: 102492. https://doi.org/10.1016/j.surfin.2022.102492

10. Alfryyan N, Munir S, Latif M, Alrowaili Z, Al-Buriahi M. Synthesis of CNT supported nickel and cobalt doped zinc ferrite for photodegradation of organic effluents by visible light irradiation. Optik. 2023; 288: 171213. https://doi.org/10.1016/j.ijleo.2023.171213

11. Azimi-Fouladi A, Falak P, Tabrizi S. The photodegradation of antibiotics on nano cubic spinel ferrites photocatalytic systems: A review. Journal of Alloys and Compounds. 2023; 961: 171075. https://doi.org/10.1016/j.jallcom.2023.171075

12. Mohammed N, Shamma R, Elagroudy S, Adewuyi A. Copper ferrite immobilized on chitosan: A suitable photocatalyst for the removal of ciprofloxacin, ampicillin and erythromycin in aqueous solution. Catalysis Communications. 2023; 182: 106745. https://doi.org/10.1016/j.catcom.2023.106745

13. Kumari S, Dhanda N, Thakur A, Gupta V, Singh S. Nano Ca–Mg–Zn ferrites as tuneable photocatalyst for UV light-induced degradation of rhodamine B dye and antimicrobial behavior for water purification. Ceramics International. 2023; 49: 12469-12480. https://doi.org/10.1016/j.ceramint.2022.12.107

14. Ravindra A, Chandrika M, Sandeep A. Superior photocatalytic performance of ancillary-oxidant-free novel starch supported nano $MFe_2O_4$ (M = Zn, Ni, and Fe) ferrites for degradation of organic dye pollutants. Surfaces and Interfaces. 2023; 41: 103180. https://doi.org/10.1016/j.surfin.2023.103180

15. Ferreira M, Bernardino E, Barros M, Bergamasco R, Yamaguchi N. An overview of nanostructured manganese ferrite as a promising visible-light-driven photocatalyst for wastewater remediation. Journal of Water Process Engineering. 2023; 54: 104049. https://doi.org/10.1016/j.jwpe.2023.104049




**Citation:** Ghoneim AI (2023) Optical spectroscopic analysis, supercapacitance, photocatalysis of $BaTi_xFe_{12-(4/3)x}O_{19}$ hexagonal nanoparticles. Open Journal of Chemistry 9(1): 006-015. DOI: https://dx.doi.org/10.17352/ojc.000031

16. Mmelesi O, Merah S, Nkambule T, Kefeni K, Kuvarega A. Synergistic role of N-doped carbon quantum dots on Zn-doped cobalt ferrite (N-CQDs/ZnCF) for the enhanced photodegradation of oxytetracycline under visible light. Materials Science and Engineering: B. 2023; 294: 116538. https://doi.org/10.1016/j.mseb.2023.116538

17. Nazir A, Imran M, Kanwal F, Latif S, Javaid A, Kim TH, Boczkaj G, Shami A, Iqbal H. Degradation of cefadroxil drug by newly designed solar light responsive alcoholic template-based lanthanum ferrite nanoparticles. Environ Res. 2023 Aug 15;231(Pt 3):116241. doi: 10.1016/j.envres.2023.116241. Epub 2023 May 25. PMID: 37244493.

18. Dhiman P, Rana G, Alshgari RA, Kumar A, Sharma G, Naushad M, ALOthman ZA. "Magnetic Ni-Zn ferrite anchored on g-$C_3N_4$ as nano-photocatalyst for efficient photo-degradation of doxycycline from water". Environ Res. 2023 Jan 1;216(Pt 3):114665. doi: 10.1016/j.envres.2022.114665. Epub 2022 Nov 9. PMID: 36334828.

19. Mahmoud M, Elshahawy A, Taha T. Lithium dopant assisted surface modification Zn ferrites for high-performance supercapacitor applications. Journal of Energy Storage. 2023; 68: 107881. https://doi.org/10.1016/j.est.2023.107881

20. Ilayas T, Anjum S, Raja M, Khurram R, Sattar M. Rietveld refinement, 3D view and electrochemical properties of rare earth lanthanum doped nickel ferrite to fabricate high performance electrodes for supercapacitor applications. Ceramics International. 2023; 49: 28864-28877. https://doi.org/10.1016/j.ceramint.2023.06.154

21. Agale P, Salve V, Patil K, Mardikar S, Uke S. Synthesis, characterization, and supercapacitor applications of Ni-doped $CuMnFeO_4$ nano Ferrite. Ceramics International. 2023; 49: 27003-27014. https://doi.org/10.1016/j.ceramint.2023.05.240

22. Alqarni A, Cevik E, Almessiere M, Baykal A, Gondal M. Fabrication of Bismuth-doped Co–Ni spinel ferrite electrodes for enhanced cyclic performance in asymmetric supercapacitors. Journal of Physics and Chemistry of Solids. 2023; 177: 111288. https://doi.org/10.1016/j.jpcs.2023.111288

23. Lashkenari M, Amir-mohammad, Ghasemi K, Khalid M, Shahgaldi S. Facile synthesis of N-doped graphene oxide decorated with copper ferrite as an electrode material for supercapacitor with enhanced capacitance. Electrochimica Acta. 2023; 465: 142959. https://doi.org/10.1016/j.electacta.2023.142959

24. urRehman A, Batool Z, Ahmad M, Iqbal M, ul-Haq A. Impact of ZnO on structural and electrochemical properties of silver spinel ferrites for asymmetric supercapacitors. Journal of Electroanalytical Chemistry. 2023; 931: 117206. https://doi.org/10.1016/j.jelechem.2023.117206

25. Jeevanantham B, Shobana M, Pazhanivel T, Choe H. Pseudocapacitive behaviors of strontium-doped cobalt ferrite nanoparticles for supercapacitor applications. Journal of Alloys and Compounds. 2023; 960: 170651. https://doi.org/10.1016/j.jallcom.2023.170651

26. Foroutan N, Lashkenari M, Alizadeh E, Sedighi M. Synthesis of manganese ferrite/graphene oxide nanocomposite and investigation of its supercapacitor behaviors. International Journal of Hydrogen Energy. 2023; 48: 25859-25868. https://doi.org/10.1016/j.ijhydene.2023.03.148

27. Anwar M, Cochran E, Zulfiqar S, Warsi M, Shakir I. In-situ fabricated copper-holmium co-doped cobalt ferrite nanocomposite with cross-linked graphene as novel electrode material for supercapacitor application. Journal of Energy Storage. 2023; 72: 108438. https://doi.org/10.1016/j.est.2023.108438

28. Somasundaram AJ, Xiao H, Pandiyarajan S, Liao AH, Lydia S, Chuang HC. In-situ fabrication of manganese ferrite grafted polyaniline nanocomposite: A magnetically reusable visible light photocatalyst and a robust electrode material for supercapacitor. J Colloid Interface Sci. 2023 Jul 15;642:584-594. doi: 10.1016/j.jcis.2023.03.170. Epub 2023 Mar 31. PMID: 37028165.

29. Ghoneim A. High Surface Area and Photo-catalysis of $Cu_{0.3}Cd_{0.7}CrFeO_4$ Nanocrystals in Degradation of Methylene Blue (MB). Egypt J. Solids. 2021; 43: 211 https://ejs.journals.ekb.eg/

30. Wu Q, Yang H, Zhu H, Gao Z. Construction of CNCs-$TiO_2$ heterojunctions with enhanced photocatalytic activity for crystal violet removal. Optik. 2019; 179: 195-206. https://doi.org/10.1016/j.ijleo.2018.10.153

31. Cullity BD. Addison-wesley puplishing company, INC. Elements of X-ray differaction. second edition. 1978.

32. Mazen S. Tetravalent ions substitution in Cu - ferrite; structure formation and electrical properties. Materials Chemistry and Physics. 2000; 62: 131-138. https://doi.org/10.1016/S0254-0584(99)00154-6

33. Kumar V, Ali Y, Sonkawade R, Dhaliwal A. Effect of gamma irradiation on the properties of plastic bottle sheet. Nucl. Instrum. Meth. Phys. Res. B. 2012; 287: 10–14. http://dx.doi.org/10.1016/j.nimb.2012.07.007

34. Patange S, Shirsath S, Lohar K, Algude S, Kamble S. Infrared spectral and elastic moduli study of $NiFe_{2-x}Cr_xO_4$ nanocrystalline ferrites. Journal of Magnetism and Magnetic Material. 2013; 325: 107-111. http://dx.doi.org/10.1016/j.jmmm.2012.08.022

35. Patange S, Shirsath S, Jadhav S, Hogade V, Kamble S. Elastic properties of nanocrystalline aluminum substituted nickel ferrites prepared by co-precipitation method. Journal of Molecular Structure. 2013; 1038: 40-44. http://dx.doi.org/10.1016/j.molstruc.2012.12.053

36. Amer M, Meaz T, Attalah S, Ghoneim A. Annealing effect on structural phase transition of as-synthesized $Mg_{0.1}Sr_{0.1}Mn_{0.8}Fe_2O_4$ nanoparticles. Journal of Alloys and Compounds. 2016; 654: 45-55. http://dx.doi.org/10.1016/j.jallcom.2015.09.114

37. Modi K, Trivedi U, Sharma P, Lakhani V, Chhantbar M. Study of elastic properties of fine particle copper-zinc ferrites through infrared spectroscopy. Indian Journal of Pure Applied Physics. 2006; 44: 165-168. http://nopr.niscair.res.in/bitstream/123456789/8255/1/IJPAP%2044%282%29%20165-168.pdf

38. Wang H, Xu L, Liu C, Jiang Z, Feng Q. A novel magnetic photocatalyst $Bi_3O_4Cl$/$SrFe_{12}O_{19}$: Fabrication, characterization and its photocatalytic activity. Ceramics International. 2019. https://doi.org/10.1016/j.ceramint.2019.08.283

39. Rayan D, Elbashar Y, Rashad M, El-Korashy A. Optical spectroscopic analysis of cupric oxide doped barium phosphate glass for bandpass absorption filter. Journal of Non-Crystalline Solids. 2013; 382: 52–56. http://dx.doi.org/10.1016/j.jnoncrysol.2013.10.002

40. Srivastava M, Chaubey S, Ojha A. Investigation on size dependent structural and magnetic behavior of nickel ferrite nanoparticles prepared by sol–gel and hydrothermal methods. Materials Chemistry and Physics. 2009; 118: 174–180. doi:10.1016/j.matchemphys.2009.07.023

41. Vinosha P, Xavier B, Anceila D, Das S. Nanocrystalline ferrite (MFe2O4, M=Ni, Cu, Mn and Sr) photocatalysts synthesized by homogeneous Coprecipitation technique. Optik. 2018; 157: 441–448. https://doi.org/10.1016/j.ijleo.2017.11.016

42. Kanna R, Lenin N, Sakthipandi K, Sivabharathy M. Impact of lanthanum on structural, optical, dielectric and magnetic properties of $Mn_{1-x}Cu_xFe_{1.85}La_{0.15}O_4$ spinel nanoferrites. Ceramics International. 2017; 43: 15868–15879. http://dx.doi.org/10.1016/j.ceramint.2017.08.160

43. Thakur P, Sharma R, Sharma V, Sharma P. Structural and Optical Properties of $Mn_{0.5}Zn_{0.5}Fe_2O_4$ Nano Ferrites: Effect of Sintering Temperature. Materials Chemistry and Physics. 2017. DOI: 10.1016/j.matchemphys.2017.02.043

44. Badran H, AL-Mudhaffer M, Hassan Q, AL-Ahmad A. Study Of The Linear Optical Properties And Surface Energy Loss Of 5',5"-Dibromo-O-Cresolsulfophthalein Thin Films.Chalcogenide Letters. 2012; 12: 483-493. http://chalcogen.ro/483_Badran.pdf

45. Ciocarlan R, Seftel E, Mertens M, Pui A, Mazaj M. Novel magnetic nanocomposites containing quaternary ferrites systems $Co_{0.5}Zn_{0.25}M_{0.25}Fe_2O_4$ (M=Ni, Cu, Mn, Mg) and $TiO_2$-anatase phase as photocatalysts for wastewater remediation under solar light irradiation. Materials Science and Engineering: B. 2018; 230: 1–7. https://doi.org/10.1016/j.mseb.2017.12.030



**Citation:** Ghoneim AI (2023) Optical spectroscopic analysis, supercapacitance, photocatalysis of $BaTi_xFe_{12-(4/3)x}O_{19}$ hexagonal nanoparticles. Open Journal of Chemistry 9(1): 006-015. DOI: https://dx.doi.org/10.17352/ojc.000031

46. Srivastava M, Mishra R, Singh J, Srivastava N, Kim N. Consequence of pH Variation on the Dielectric Properties of Cr-doped Lithium Ferrite Nanoparticles Synthesized by the Sol-gel Method. Journal of Alloys and Compounds. 2015. http://dx.doi.org/10.1016/j.jallcom.2015.05.017

47. Rezaie E, Rezanezhad A, Ghadimi L, Hajalilou A, Arsalani N. Effect of calcination on structural and supercapacitance properties of hydrothermally synthesized plate-like $SrFe_{12}O_{19}$ hexaferrite nanoparticles. Ceramics International. 2018; 44: 20285–20290. https://doi.org/10.1016/j.ceramint.2018.08.014

48. Rajaji U, Chinnapaiyan S, ChenT, Chen S, Mani G. Rational construction of novel strontium hexaferrite decorated graphitic carbon nitrides for highly sensitive detection of neurotoxic organophosphate pesticide in fruits. Electrochimica Acta. 2021; 371: 137756. https://doi.org/10.1016/j.electacta.2021.137756

49. Ghoneim A, Matsuda A. Thermal Analysis and Electrochemical Performance of Mn doped Cu Nano-ferrites. Egyptian Journal of Solids. 2021; 43: 37-60. https://ejs.journals.ekb.eg/

50. Ghoneim A, Matsuda A, Tan W. Structural, Thermal and Electrochemical studies of Sm substituted $CrFeO_3$ Nano-Pervoskites. Journal of Alloys and Compounds. 2021; 870: 159420. https://doi.org/10.1016/j.jallcom.2021.159420





**Citation:** Ghoneim AI (2023) Optical spectroscopic analysis, supercapacitance, photocatalysis of $BaTi_xFe_{12-(4/3)x}O_{19}$ hexagonal nanoparticles. Open Journal of Chemistry 9(1): 006-015. DOI: https://dx.doi.org/10.17352/ojc.000031